

Experimental analysis of flow pattern and heat transfer in circular-orifice baffled tubes

J. Muñoz-Cámara^{a,*}, D. Crespí-Llorens^b, J.P. Solano^a, P.V. Quiles^b

^a*Dep. Ingeniería Térmica y de Fluidos, Universidad Politécnica de Cartagena
Campus Muralla del Mar (30202) Cartagena, Spain*

^b*Universidad Miguel Hernández. Departamento de Ingeniería Mecánica y Energía, Avda.
de la Universidad s/n, 03202, Elche, Spain*

Abstract

An experimental study on the thermal-hydraulic and flow pattern characteristics of tubes with circular-orifice baffled inserts is performed. A geometry with an orifice-to-tube diameter ratio of $d/D = 0.5$ and an interbaffle spacing equal to $1.5 D$ is tested in steady-state conditions. Isothermal friction factor tests in the range $10 < Re < 2200$ allow the laminar, transitional and turbulent flow regimes to be identified. Flow visualization by means of hydrogen bubbles is used to assess the main flow structures and their relation with the onset of transition, which occurs at $Re \approx 160$. Heat transfer experiments under uniform heat flux are conducted in order to obtain the Nusselt number as a function of Reynolds number, for $150 < Pr < 630$, using propylene-glycol as the test fluid. Numerical simulations are used to complement the visualization study and explain the role of the flow structures on the thermal-hydraulic behavior.

Keywords: heat transfer enhancement, turbulence promoters, transitional

*Corresponding author

Email address: jose.munoz@upct.es (J. Muñoz-Cámara)

1 **Nomenclature**

2	c_p	specific heat ($\text{J kg}^{-1} \text{K}^{-1}$)
3	C_0	orifice coefficient (-)
4	d	orifice diameter (m)
5	D	tube inner diameter (m)
6	k	thermal conductivity ($\text{W m}^{-1} \text{K}^{-1}$)
7	l	Tube length (m)
8	l_{rec}	recirculation length (m)
9	L	distance between consecutive baffles (m)
10	L_h	heated length (m)
11	L_p	distance between pressure ports (m)
12	\dot{m}	mass flow rate (kg/s)
13	N	number of tubes (-)
14	q	net heat transfer rate (W)
15	q''	net heat flux (W/m^2)
16	$R3$	performance evaluation criterion (-)
17	S	open area, $(d/D)^2$ (-)
18	t	Baffle thickness (m)
19	T	Temperature ($^{\circ}\text{C}$)
20	u	mean velocity, based on the tube diameter, D (m)
21	\dot{W}	power consumption (W)
22	x	axial distance from the start of the heated area (m)
23	Δp	pressure drop (Pa)

24

25 *Dimensionless groups*

26 f Fanning friction factor, $\frac{\Delta p}{2\rho u^2} \frac{D}{L}$

27 Gr Grashof number, $g\beta q'' D^4 / k\nu^2$

28 Nu Nusselt number, hD/k

29 Pr Prandtl number, $\mu c_p / k$

30 Re Reynolds number, $\rho v D / \mu$

31

32 *Greek symbols*

33 β coefficient of thermal expansion (K^{-1})

34 μ dynamic viscosity ($kg\ m^{-1}\ s^{-1}$)

35 ν kinematic viscosity ($Pa\ s$)

36 ρ fluid density ($kg\ m^{-3}$)

37 σ standard deviation

38

39 *Subscripts*

40 b bulk

41 in inlet

42 j section number

43 s smooth tube

44 wi inner wall

45

46 1. Introduction

47 Insert devices are widely used means of heat transfer enhancement, which
48 can be installed in smooth tubes of heat exchangers while maintaining their
49 original mechanical strength. Likewise, retrofitting of existing equipment
50 with tube inserts is also a remarkable advantage of this type of devices.
51 Twisted tapes [1, 2, 3], wire coils [4, 5] and wire meshes [6] are typical designs
52 used as insert devices in heat exchangers. Their geometrical characteristics
53 must be chosen according to the operational conditions of the internal flow,
54 in order to maximize convective heat transfer enhancement, keep pressure
55 drop under reasonable levels and -if applicable- achieve turbulent promotion
56 at low Reynolds number. Equally-spaced circular rings are another typology
57 of insert device, where convective heat transfer is augmented on the basis of
58 the periodic contraction and expansion of the bulk flow. They consist of flat
59 disks with a central orifice, whose open area fraction is typically characterized
60 by the orifice-to-tube diameter ratio d/D .

61 A limited number of experimental studies have analyzed the thermal-hydraulic
62 performance of circular rings. Kongkaietpaiboon et al. [7] studied the heat
63 transfer and pressure drop for circular-ring turbulators, testing several diam-
64 eter ratios ($d/D = 0.5, 0.6$ and 0.7) and three pitch ratios, L/D (free space
65 between baffles divided by the tube inner diameter), achieving a maximum
66 thermal performance of 7% for the lowest pitch ratio ($L/D = 6$) and the high-
67 est d/D value. Promvonge et al. [8] tested inclined annular baffles, varying
68 the relation between the disk thickness and the tube diameter, and the pitch
69 ratio (0.5, 1.0, 1.5, 2.0) for an angle of 30° . A maximum value of 40% was
70 found for the thermal performance for the lowest thickness/diameter ratio

71 and the lowest pitch ratio. Acir et al. [9] studied heat transfer in tubes with
72 annular disks, focusing on the effect of the pitch ratio L/D , and the number
73 of orifices over the annulus; a maximum thermal performance of 83% was
74 found for the geometry with two orifices and $L/D = 2$. Ruengpayungsak
75 et al. [10] modified the annular geometry to include some semi-circular ori-
76 fices to achieve a gear-ring geometry; a maximum thermal performance for
77 $L/D = 3$ of 24%, 26%, 28% and 30% was found for baffles with tooth numbers
78 of 0, 8, 16 and 24. In addition, circular-rings have been used in combination
79 with other geometries as twisted tapes. Eiamsa-ard et al. [11] studied the
80 thermal performance of a tube with twisted-tape and circular ring inserts.
81 Several twist ratios (3.0, 4.0 and 5.0) and pitch ratios (1.0, 1.5 and 2.0) were
82 tested. The maximum thermal performance, 42%, was achieved at the lowest
83 twist and pitch ratios and Reynolds number tested ($Re \approx 6000$). Abolarin
84 et al. [12] tested u-cut twisted tapes with ring inserts, obtaining earlier tran-
85 sitions and an increase in the pressure drop and the heat transfer when the
86 rings were inserted, and the distance between them was lower.
87 From these studies, it can be concluded that these inserts show a high thermal
88 performance when their geometry is well selected. It is also remarkable that
89 all of them detected the highest thermal performance at the lowest Reynolds
90 number of their tests, which were in almost all cases above $Re = 3000$. How-
91 ever, many industrial applications that may require the use of insert devices
92 for heat transfer enhancement purposes work in laminar or transitional flow
93 regimes and high Prandtl number fluids. Furthermore, the effect of Prandtl
94 number on heat transfer in tubes with circular rings is not reported in the
95 open literature, as the majority of experiments only use air as test fluid.

96 In addition to the interest of circular rings as a passive technique, these
97 inserts have spread their applications during the last decades, due to the
98 potential benefit in enhancing mass and heat transfer when an oscillatory
99 flow is superimposed to a net flow. Currently, this configuration is found in
100 oscillatory-baffled reactors (OBR), where the inserts promote the continuous
101 flow separation and reattachment. In OBRs, a high-residence time product
102 flows across the circular tube, yielding very low net flow Reynolds numbers.
103 A piston or bellow connected to the tube provides a superimposed oscillatory
104 flow, which increases the radial mixing and promotes heat and mass transfer
105 intensively [13]. A few number of experimental investigations have shed
106 light on the heat transfer characteristics of OBRs with circular orifice baffles
107 [14, 15, 16]. However, the performance of the tube insert in the absence of
108 oscillatory flow is still insufficiently described, correlations for Nusselt number
109 are available only for the turbulent region (Reynolds numbers above 200) and
110 the role of the Prandtl number has not been studied properly. In addition,
111 González-Juárez et al. [17] studied numerically the heat transfer in baffled
112 tubes and reported unrealistic behaviors for the proposed correlations [14, 15]
113 after extrapolating at lower Reynolds numbers, because these provided lower
114 heat transfer rates than a smooth tube. The need to increase the studied
115 range of Reynolds numbers is justified by some potential applications, where
116 the required residence time could be higher, or the fluid has a very high
117 viscosity.

118 The experimental analysis of the flow pattern in circular rings has also at-
119 tracted little attention up to date. Kiml et al. [18] performed heat transfer
120 and visualization tests in tubes with transverse and inclined circular rings,

121 with $d/D = 0.8$, working in the Reynolds number range [5000 – 20000].
122 Focusing on the transverse ribs, they identified the separation bubbles just
123 behind the ribs and the reattachment point between consecutive ribs. This
124 flow pattern showed a clear influence on the local Nusselt number results;
125 after the flow separation downstream the rib, a sharp drop in heat transfer
126 was noticed past the reattachment point due to the boundary layer growth.
127 Muñoz et al. [19] used the Particle Image Velocimetry technique to study the
128 behavior of the flow in equally-spaced baffles in round tubes with $d/D = 0.5$,
129 $L/D = 1.5$ and $20 < Re < 300$. The measurement of the turbulent intensity
130 and the energy of the fluctuating components of the flow field allowed to
131 assess the unstable nature of the flow for $Re > 160$.
132 Experimental correlations for Fanning friction factor in the low Reynolds
133 number range (e.g. $Re < 3000$) have not been reported so far in the open
134 literature. An attempt to quantify the steady-state pressure drop in net
135 and oscillatory superimposed flows was accounted for in the quasy-steady
136 model proposed by Jealous and Johnson [20]. This model assumes that the
137 pressure drop caused by a steady-state flow along a tube with equally-spaced
138 annular baffles is the same as a series of individual orifices in a turbulent
139 flow, using the discharge coefficient concept. This approach presents two
140 main drawbacks: a) the discharge coefficient is strongly influenced by the flow
141 regime [21], particularly in the laminar and transitional ranges, which advises
142 against the use of a constant discharge coefficient in some applications; b)
143 the interaction of the flow between consecutive baffles is not accounted for if
144 the discharge coefficient is used for evaluating the overall pressure drop.
145 The present study aims at clarifying some open questions on the thermal-

146 hydraulic characteristics and flow mechanisms in tubes with equally-spaced
147 annular baffles working in the laminar and transitional flow regimes. A baffle
148 geometry with $d/D = 0.5$ and pitch ratio $L/D = 1.5$ is used as test speci-
149 men, following the widely accepted designs for the construction of oscillatory
150 baffled reactors proposed by Ni et al. [22]. Heat transfer tests under uniform
151 heat flux conditions are conducted for a range of net-flow Reynolds number
152 $10 < Re < 3000$, using propylene-glycol as working fluid at different tem-
153 peratures, which allows to extend the Prandtl number analysis to the range
154 $150 < Pr < 630$. Friction factor measurements obtained under isothermal
155 conditions are presented in the range $10 < Re < 3000$, allowing the transi-
156 tion from laminar to turbulent flow to be identified. The physics of transition
157 are described experimentally using hydrogen bubble visualization, and CFD
158 results are also employed to support the discussion of the impact of the flow
159 structures on the thermohydraulic behaviour.

160 **2. Experimental test rig**

161 *2.1. Geometry*

162 The geometry under study is shown at Fig. 1. The insert baffles are a geomet-
163 rical annuli fitted to the inner tube wall, with an orifice diameter $d = 0.5D$.
164 The baffle spacing is $1.5D$. The baffles are made of PEEK plastic (to avoid
165 electrical conduction from the tube wall) with thickness $t = 1mm$. They are
166 assembled using three axial rods (1.6 mm diameter).

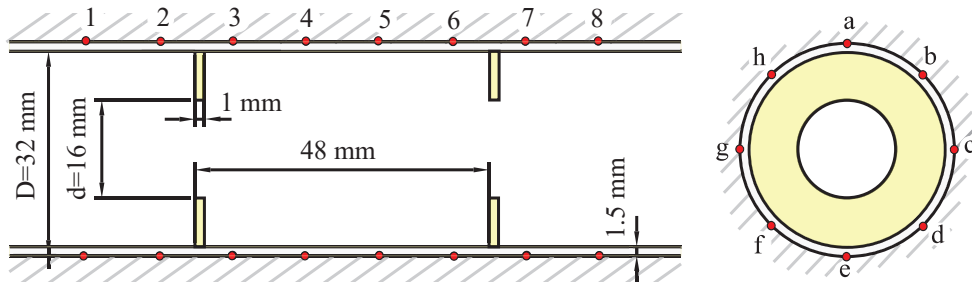


Figure 1: Baffle geometry and thermocouple arrangement in the test section.

167 *2.2. Visualization facility*

168 The facility depicted in Fig. 2 was built in order to study the flow within the
 169 described geometry by using hydrogen bubble visualization.

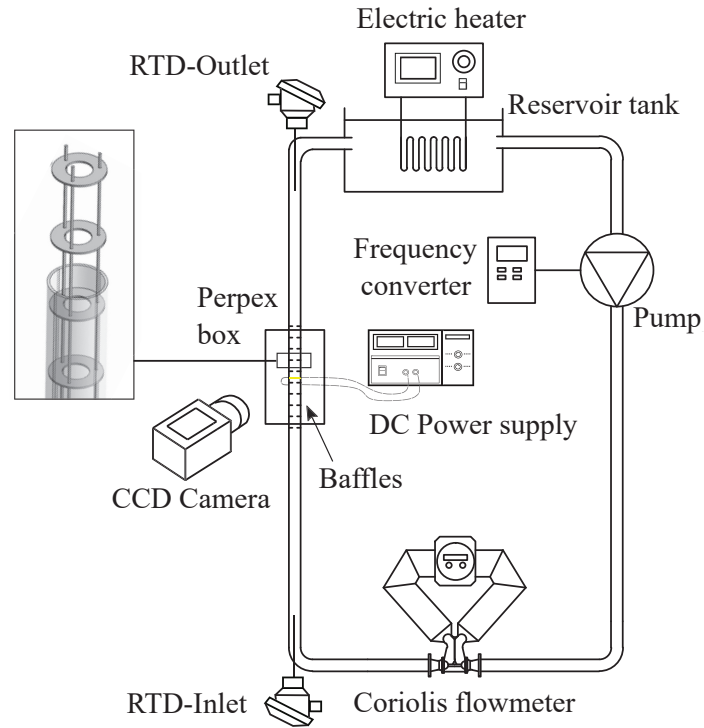


Figure 2: Experimental setup for hydrogen bubble visualization.

170 The test section consists of a $D = 32$ mm diameter acrylic tube (also depicted
 171 at Fig. 2) equally spaced insert baffles which are fixed by three steel rods. The
 172 use of the rods has been avoided in the visualization section for better results.
 173 Five baffles are placed upstream of the test section and also downstream of
 174 it in order to ensure spatial periodicity of the flow field. A flat-sided acrylic
 175 box, filled with the same working fluid used in the facility, is placed around
 176 the test section for a better optical access.
 177 Heating and final temperature control is carried out by an electric heater
 178 located in the upper reservoir tank. A Coriolis flowmeter and a control valve
 179 are used to control and monitor the working flow rate.

180 The visualization by hydrogen bubbles is a qualitative technique that allows
181 the perception of the main flow structures. For that, the hydrogen bubbles
182 are generated by means of a copper wire (cathode) that crosses the tube
183 diametrically upstream of the visualization area, being the anode a metallic
184 component of the circuit located downstream of the test section. Thus, a
185 symmetry plane of the flow is seeded with hydrogen bubbles, while illumina-
186 tion is provided by two rear lamps. A CMOS 1280x1024 pix² CMOS camera
187 is situated in orthogonal position in relation to that plane, so that it can have
188 a front view of it, or in parallel to it in order to have a side view. The bubbles
189 size and quantity are set up by adjusting the direct current voltage applied
190 between cathode and anode. Finally, In order to work with feed voltages
191 below 50 V, the electrical conductivity of the working fluid is increased by
192 adding salt.

193 *2.3. Thermal-hydraulic tests*

194 A schematic diagram of the experimental set-up is shown in Fig. 3. It consists
195 of three independent circuits. The second and third circuits are used to
196 regulate the temperature of the reservoir tank (1). Test fluid was pumped
197 from the open reservoir tank (1) by a train of three variable-speed gear pumps
198 (2). The flow rate was measured by a Coriolis flow-meter (3). The baffles
199 are installed in the main circuit (5). The test section was a thin-walled, 2
200 m long, 316L stainless steel tube with 37 equally-spaced insert baffles. The
201 inner and outer diameters of the tube were 32 mm and 35 mm, respectively

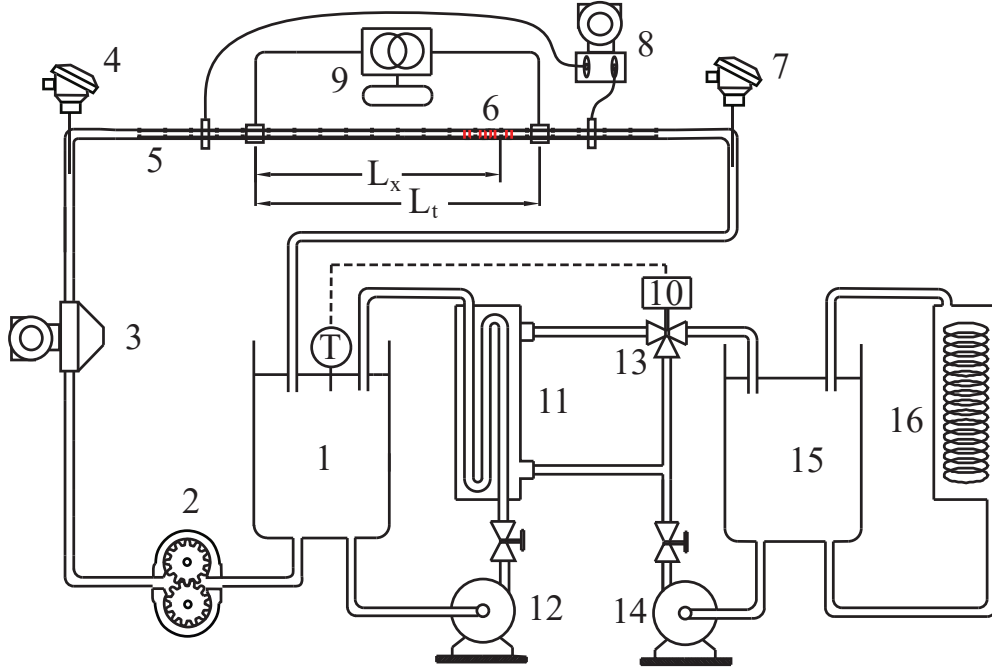


Figure 3: Experimental set-up. (1) Reservoir tank, (2) Pumping system, (3) Coriolis Flowmeter, (4) PT-100 Class B 1/10 DIN temperature sensors, Inlet, (5) Baffles, (6) Wall thermocouples, (7) PT100, Outlet, (8) Pressure transducer, (9) Autotransformer, (10) PID Controller, (11) Heat Exchanger, (12) Centrifugal Pump, (13) Three way valve, (14) Centrifugal Pump, (15) Reservoir tank, (16) Chiller.

202 Heat transfer experiments were carried out under uniform heat flux (UHF)
 203 conditions. The tube was heated by Joule effect through AC in the tube
 204 wall. Power was supplied by a 6 kVA transformer (9) connected with copper
 205 electrodes to the tube. A variable auto-transformer was used for power regu-
 206 lation. The loop was insulated by an elastomeric thermal insulation material
 207 to minimize heat losses. The overall electrical power added to the heating
 208 section was calculated by measuring the voltage between electrodes and the

209 electrical current. Fluid inlet (4) and outlet (7) temperatures were measured
210 by submerged type RTDs (Resistance Temperature Detector).

211 Fig. 1 shows the wall temperature measurement lay-out installed along the
212 test section, using T-type thermocouples. The measurement section is lo-
213 cated 13 cell tanks downstream of the first electrode, to ensure that the flow
214 is thermally developed (spatially-periodic). A total number of 64 thermo-
215 couples peripherally distributed along eight axial sections on the outside wall
216 cover two consecutive mixing tanks, following the sketches of Fig. 1. This
217 arrangement is aimed at detecting the circumferential temperature gradient
218 due to the flow stratification in the laminar region, and the axial temperature
219 variations due to the local flow characteristics that occur between consecutive
220 baffles. Pressure drop tests were carried out under isothermal conditions. In
221 order to capture the characteristics of the spatially-periodic flow, the first
222 pressure port is placed in the fifth inter-baffle spacing. The second pressure
223 port is located in the twenty-seventh inter-baffle spacing, which falls at a
224 distance $L_p = 1.296$ downstream. Four pressure holes separated by 90° are
225 made in the pressure connections in order to accommodate any peripheral
226 disturbances of the static pressure. A set of highly accurate capacitive dif-
227 ferential pressure transducers (range: 0-10 mbar, 0-50 mbar, 5-500 mbar,
228 22-2500 mbar) were employed to measure the pressure drop along the test
229 section. Propylene-glycol is used as working fluid. To ensure the right char-
230 acterization of the fluid viscosity, a calibrated Cannon-Fenske viscometer is
231 used periodically. The fluid temperature in the main tank is regulated by
232 two additional circuits, with a variation of 0.1°C of the target temperature.

233 *2.4. Data reduction*

234 Two different calibration tests were performed in order to conduct the heat
235 transfer experiments appropriately. Firstly, calibration of the wall thermo-
236 couples was achieved by circulating very high flow rates of fluid at different
237 temperatures. Steady-state measurements of the inlet and outlet tempera-
238 tures and evaluation of the conduction thermal resistances across tube wall
239 and insulation, allowed us to calibrate them, taking into account any contact
240 resistance with the tube wall. Secondly, heat losses to the ambient were eval-
241 uated by measuring the fluid inlet and outlet temperatures when low flow
242 rates were circulated through the test section at different temperatures. The
243 circumferential average Nusselt number is calculated at each section, j , using
244 the following expression:

$$\bar{N}u_j = \frac{q''}{\bar{T}_{w,i,j} - T_{b,j}} \cdot \frac{D}{k} \quad (1)$$

245 where q'' is the generated heat (the voltage times the electric current) minus
246 the heat losses along the test section, per heated area. $T_{w,i,j}$ is the aver-
247 aged inner wall temperature at the j section, which is calculated using a
248 two-dimensional numerical model which solves the radial and axial heat con-
249 duction equation in the tube wall. $T_{b,j}$ is the bulk fluid temperature at the
250 section j . Since the heat was added uniformly along the tube length, $T_{b,j}$ was
251 calculated by considering a linear variation with the axial direction, according
252 to:

$$T_{b,j} = T_{b,in} + \frac{q}{\dot{m}c_p} \cdot \frac{x_j}{L_h} \quad (2)$$

253 where $T_{b,i}$ is the fluid temperature at the inlet of the test section and x_j is the
 254 axial distance between the test section j and the point where the tube heating
 255 starts. The circumferential average Nusselt number is corrected by the factor
 256 $(\mu_{w_i}/\mu_{w_b})^{0.14}$ to account for the change in the physical properties due to the
 257 temperature radial gradient [23]. Finally, the axial-averaged Nusselt number
 258 is calculated as:

$$\bar{N}u = \frac{\sum_1^8 \bar{N}u_j}{8} \quad (3)$$

259 Fanning friction factor was determined from the fluid mass flow rate and the
 260 pressure drop measurements as:

$$f = \frac{\rho \pi^2 D^5 \Delta p}{32 \dot{m}^2 L_p} \quad (4)$$

261 2.5. Uncertainty analysis

262 The experimental uncertainty was calculated by following the Guide to the
 263 expression of uncertainty in measurement' published by ISO [24]. Instrumentation
 264 errors are summarized in Table 1. Uncertainty calculations based on a
 265 95% confidence level showed limit values of 5.4% for Reynolds number, 3.9%
 266 for Prandtl number, 6.3% for Fanning friction factor and 2.3% for Nusselt
 267 number.

268 3. Numerical model

269 A 3D model of a tube with eight equally-spaced baffles is created and meshed
 270 using structured, hexahedral grid. A double compression ratio was intro-
 271 duced in both sides of the baffles, where greater variations of the flow pattern

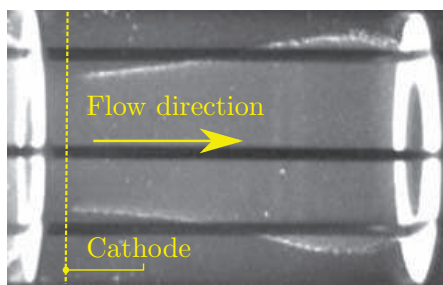
Measurement	Uncertainty
Bulk temperature	0.15 °C
Wall temperature	1.12 °C
Voltage	0.04% measure + 0.03% full scale
Intensity	0.1% measure + 0.04% full scale
Viscosity	3% measure
Pressure drop	0.2% measure
Thermal conductivity	0.9% measure
Specific heat	0.3% measure
Tube diameter	0.1% measure
Heat transfer section	0.01 m
Thermocouples position	0.005 m
Pressure test section	0.005 m

Table 1: Measurement uncertainties

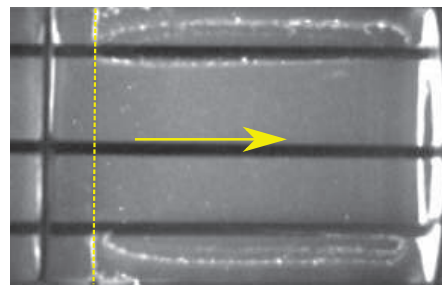
272 were expected due to the geometry constriction, and in radial direction, to
273 ensure better solution where higher-velocity gradients were expected. The
274 finite volume software ANSYS Fluent 18 was employed for the solution of
275 the continuity and momentum pressure-based equations. Full Navier-Stokes
276 equations were treated in general, body fitted coordinates. A control-volume
277 storage scheme was employed where all variables were stored at the cell cen-
278 ter. A second order upwind scheme was used in order to interpolate the face
279 values of computed variables. An implicit segregated solver solved the gov-
280 erning equations sequentially. In this study the pressure-velocity coupling
281 algorithm SIMPLE was used. Steady-state simulations were solved in a first
282 attempt, followed by the solution of the unsteady problem over a total time
283 $t = 10$ s, using a time step $\Delta t = 0.1$ s, with a second-order discretization.
284 This ensured a better convergence of the problem.

285 4. Flow visualization results

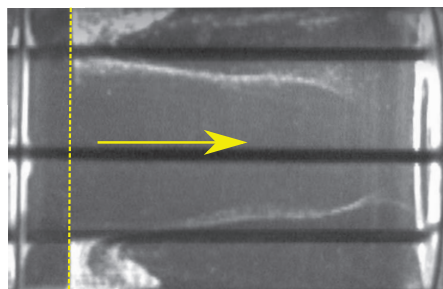
286 Experiments were carried out for Reynolds numbers between $25 < Re < 410$.
287 The results are shown at Fig. 4 and Fig. 5 in front and lateral views.
288 In Fig. 4(a), the front view for $Re = 25$, a core jet can be observed down-
289 stream the baffle, which gets broader along the cell and then narrower again
290 upstream the next baffle. Besides, low velocities are detected in the periph-
291 eral region. For $Re = 120$ the core jet has an uniform diameter along the
292 interbaffle space, which is equal to the baffles orifice diameter, d . In Fig. 4(b),
293 the bubbles generation was adjusted to show the recirculation of the outer
294 region of the flow, which, again, has much lower velocities than the jet. By
295 comparing the results for $Re = 25$ and $Re = 120$, the recirculation in the



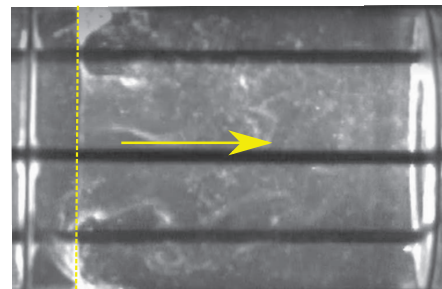
(a) $Re = 25$.



(b) $Re = 120$.

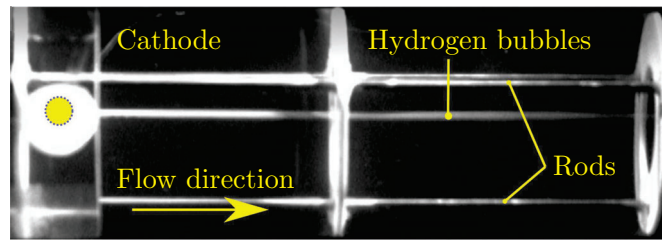


(c) $Re = 160$.

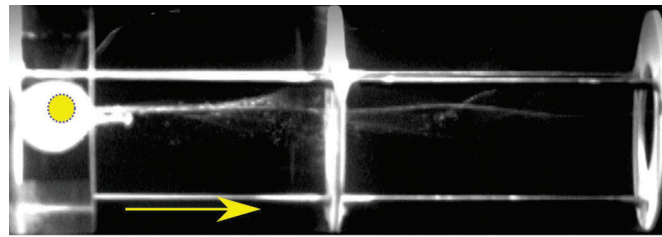


(d) $Re = 300$.

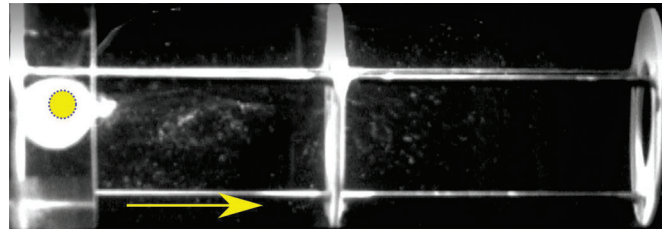
Figure 4: Front view of the flow seeded with hydrogen bubbles for different Reynolds numbers.



(a) $Re = 45$.



(b) $Re = 240$.



(c) $Re = 410$.

Figure 5: Lateral view of the flow seeded with hydrogen bubbles for different Reynolds numbers.

296 outer region of the flow is observed to grow with the Reynolds number. The
297 results for this range of Reynolds numbers ($Re < 120$) show laminar flow
298 conditions. This can be clearly detected from the lateral view of the flow
299 depicted in Fig. 5(a), where the hydrogen bubbles remain in the same plane.
300 At Reynolds number $Re = 160$ (Fig. 4(c)), a similar core jet dominates the
301 flow, although significant pulsations are detected. Such pulsations are also
302 observed, in a higher frequency, in the lateral view for $Re = 240$ in Fig. 5(b),
303 where they result in part of the bubbles coming out of the symmetry plane.
304 For higher Reynolds numbers the flow becomes chaotic. The front view of the
305 flow field for $Re = 300$, depicted in Fig. 4(d), shows no appreciable pattern
306 but a disordered flow, while the lateral view provides qualitative information
307 about a high mass transfer taking place in radial direction. The same flow
308 behaviour is observed in the experiment at $Re = 410$ in Fig. 5(c).

309 ***Text for electronic version only:*** The corresponding videos to the pre-
310 vious images can be also visualized. They show the front view of the flow
311 seeded with hydrogen bubbles for: $Re = 25$ (Video 1), $Re = 120$ (Video
312 2), $Re = 160$ (Video 3) and $Re = 300$ (Video 4), and the lateral view for
313 $Re = 45$ (Video 5), $Re = 240$ (Video 6) and $Re = 410$ (Video 7).

314 5. Numerical results

315 As could be observed in the previous section, the flow pattern seems to play a
316 key role at low Reynolds numbers before the onset of the transition. The flow
317 pattern is studied in more detailed in this subsection. So, several simulations
318 have been performed in the laminar regime, from $Re = 1$ to $Re = 150$. The
319 results, showing the velocity magnitude and the streamlines for a meridional

320 plane along a cell (space between baffles), are represented in Fig. 6 for four
321 Reynolds numbers.

322 For the lowest Reynolds number simulated (Fig. 6 (a)), $Re = 1$, the core
323 stream expands after flowing through the baffle growing up to the walls.
324 Despite the low Reynolds number, a tiny recirculation can be already seen
325 downstream the baffles. For $Re=15$, Fig. 6 (b), the core stream still reaches
326 the wall after expanding, but the recirculation has grown substantially. A
327 limit case can be seen at $Re = 32$, Fig. 6 (c), the core stream is not able
328 to fully expand before reaching the next baffle. The recirculation fills more
329 than one half of the interbaffle spacing. The extreme case corresponds to the
330 pattern at $Re = 102$, Fig. 6 (d), the core stream expands very slightly, and
331 the recirculation fills all the space between consecutive baffles, this way, the
332 flow can be described as a short-circuit between baffles.

333 In order to quantify the evolution of the size of the recirculation area, the
334 recirculation size is calculated by measuring the average distance from the
335 baffle for which the axial velocity reverses. A non-dimensional definition of
336 this size for different Reynolds number is presented in Fig. 7. The graph
337 shows a growth of the recirculation bubble with the Reynolds number, which
338 ranges from a tiny size ($l_{rec}/D = 0.04$) at $Re = 1$ to the maximum achievable
339 value, which is the interbaffle spacing, at $Re = 70$.

340 **6. Thermal-hydraulic results**

341 *6.1. Pressure drop*

342 In this subsection, the main pressure drop results are presented for Reynolds
343 numbers from $Re = 7$ to $Re = 3000$, and the different flow regions are

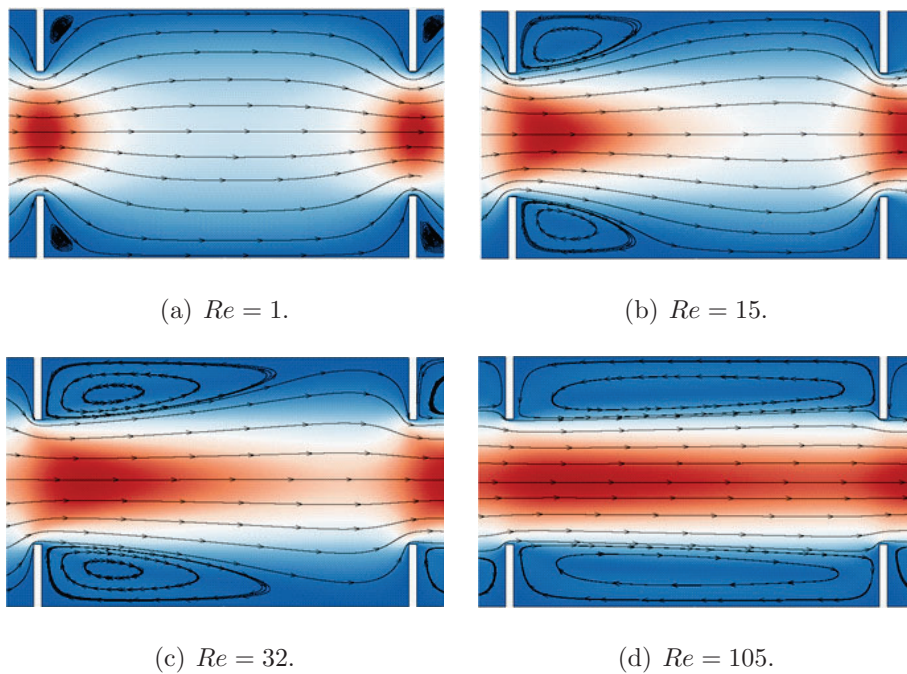


Figure 6: CFD contour of non-dimensional velocity, v/v_{med} in the symmetry plane of the OBR.

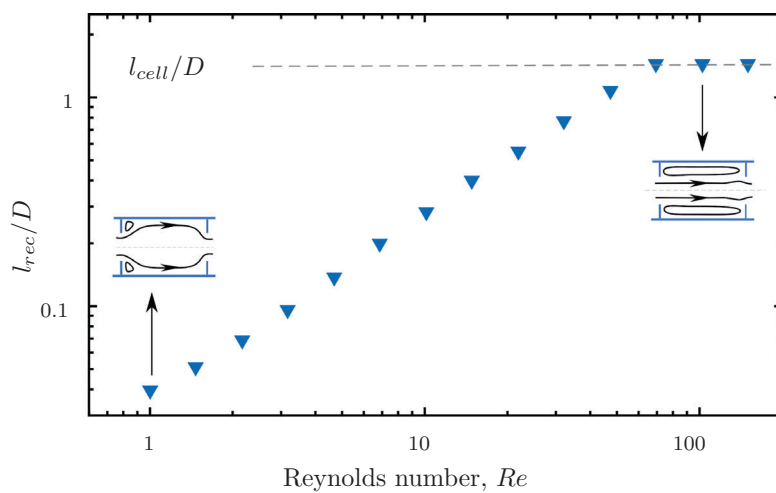


Figure 7: Recirculation zone size as a function of the Reynolds number.

344 identified. Fig. 8 (a) shows experimental results of the Fanning friction factor
345 versus the Reynolds number for the geometry under study. The analytical
346 solution for a smooth tube in laminar regime and the result obtained for an
347 orifice plate, with an orifice coefficient equals to 0.8, are represented as well.
348 The standard deviation of the pressure drop signal, sampled at a frequency
349 $f = 2$ Hz, is also presented in Fig. 8 (b). The analysis of both results allow
350 to distinguish three different flow regions:

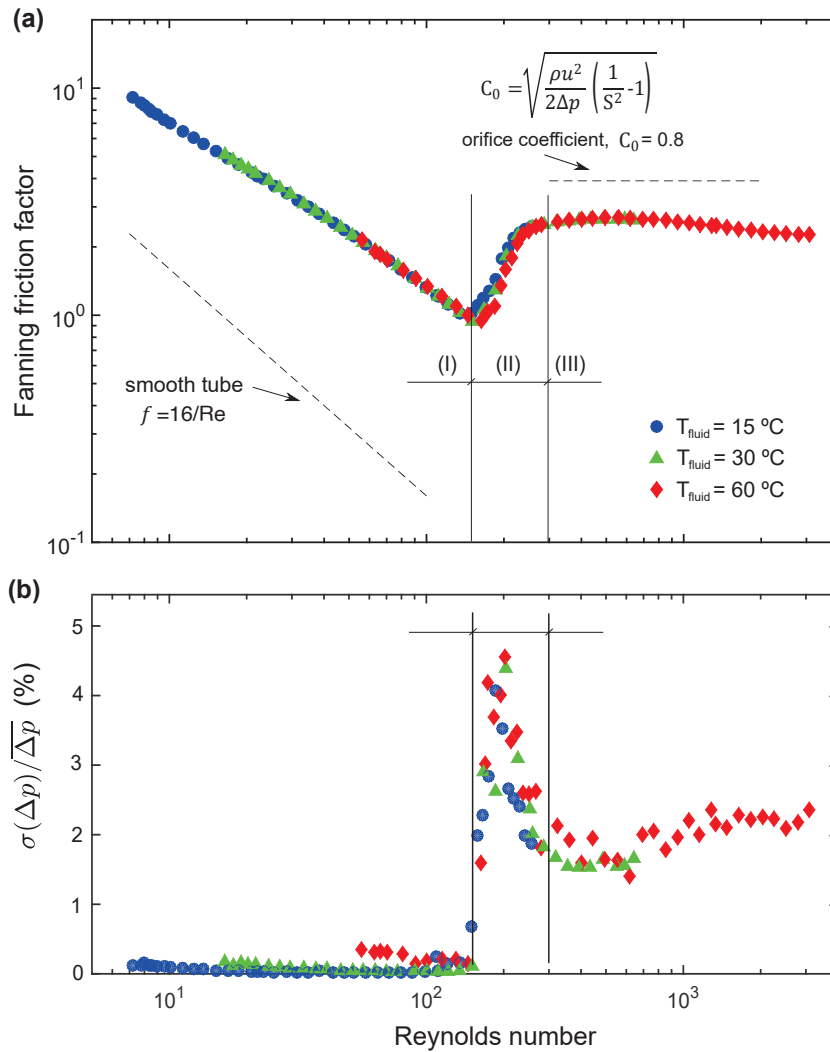


Figure 8: Fanning friction factor as a function of the Reynolds number for several tested fluid temperatures.

351 Region I: $Re < 160$

352 In this region, the flow presents characteristics of laminar flow, with a strong
 353 influence of the Reynolds number on the friction factor, what agrees with

354 the visualization results showed in Section 4. Likewise, the low fluctuation of
 355 the pressure drop signal -which is the lowest among all the regions- is a good
 356 measure of the steadiness of the flow. Besides, friction factor augmentations
 357 of about 8 times, compared to the smooth tube, are identified. Pressure drop
 358 in this region can be estimated by the following correlation, which matches
 359 the experimental results with an accuracy of 10%:

$$f = 36.5 Re^{-0.709} \quad 7 < Re < 160 \quad (5)$$

360 Region II: $160 < Re < 300$

361 An abrupt change in friction factor in this region indicates the onset of tran-
 362 sition to turbulence. Intense fluctuations of the pressure drop signal are
 363 identified in Fig. 8 (b), which correspond to the unstable behavior that has
 364 also been detected in the flow visualization tests for the same operational
 365 regime (see Figs. 4c and 5b, and the corresponding videos).

366 Region III: $Re > 300$

367 The turbulent flow regime is achieved from $Re \approx 300$ onwards. The standard
 368 deviation of the pressure signal is stabilized, with higher values than those
 369 of the laminar flow regime. The low influence of the Reynolds number on
 370 friction factor is also noticeable. The following correlation is proposed for
 371 the range $300 < Re < 3000$, which meets all the experimental results with
 372 an accuracy of 8%:

$$f = 3.14 Re^{-0.033} \quad 300 < Re < 3000 \quad (6)$$

373 As reflected in Fig. 8 (a), the friction factor is much lower than the one
 374 expected for an orifice with the same open area ratio. This can be justified

375 by the interaction between consecutive baffles, after crossing a baffle the
376 flow is not developed before reaching the next one, so the effect can not be
377 described as a series of independent baffles.

378 *6.2. Heat transfer*

379 In this subsection, the main heat transfer results are provided for Reynolds
380 numbers from 10 to 2200, and Prandtl numbers from 150 to 630. Fig. 9 shows
381 experimental results of the Nusselt number as a function of the Reynolds
382 number for three Prandtl numbers, $Pr = 150, 285$ and 630 . Based on the
383 influence of Reynolds number, three different flow regions can be clearly
384 distinguished: laminar, transitional and turbulent. In the laminar region
385 ($Re < 160$) there is a low influence of the Reynolds number on heat transfer
386 coefficients are significantly higher than those that would be obtained for
387 a smooth tube working under mixed convection conditions. The Reynolds
388 number influence is quite sharp in the transitional region ($160 < Re < 300$).
389 Onwards, the onset of turbulence highly increases the heat transfer rates.
390 This outbreak occurs for $Re > 300$, which proves the suitability of the insert
391 baffles as turbulence promoters for heat transfer increment purposes.

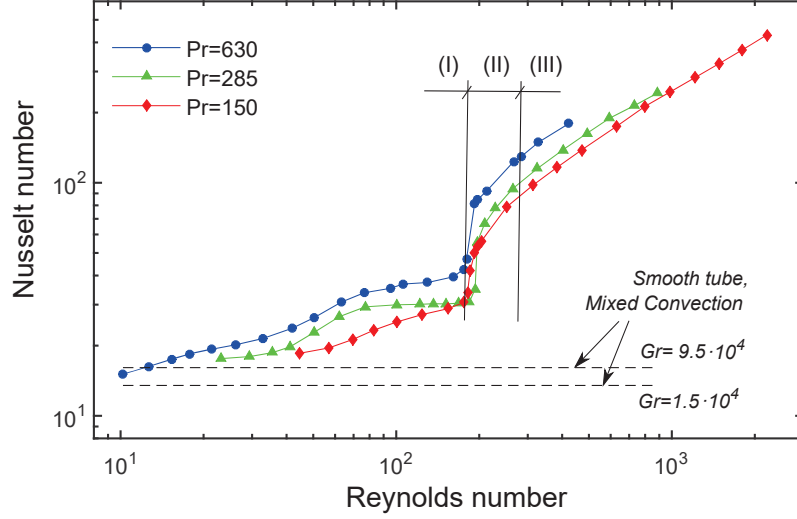


Figure 9: Nusselt number vs Reynolds number for three Prandtl numbers.

392 These data can be adjusted to correlations which as well show the influence of
 393 the Reynolds and Prandtl numbers on the Nusselt number. Eq. 7 corresponds
 394 to region I (laminar) and Eq. 8 to region III (turbulent).

$$Nu = 1.304 Re^{0.402} Pr^{0.227} \quad 10 < Re < 100 \quad (7)$$

$$Nu = 0.503 Re^{0.735} Pr^{0.216} \quad 300 < Re < 2200 \quad (8)$$

395 These equations are suitable for the Prandtl number range $130 < Pr < 650$.
 396 The exponent of the Prandtl number is similar for both regions (considering
 397 the experimental error). The fitting is quite satisfactory for both regions,
 398 with all the experimental results included in a range of $\pm 10\%$ of the corre-
 399 lation, as can be seen in Fig. 10.

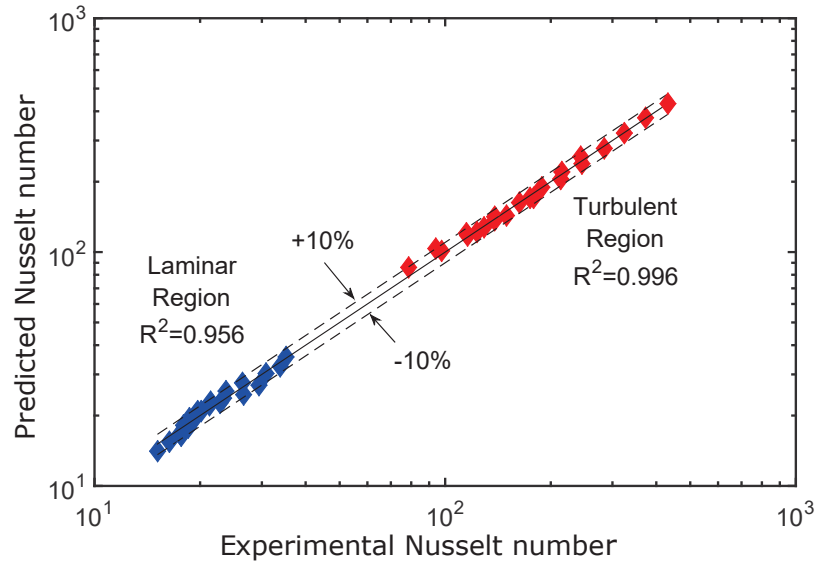


Figure 10: Comparison of the experimental Nu number and the predicted Nu number using Eq. 7 and 8.

400 A different way to identify the end of the laminar flow regime is using the
 401 standard deviation of the wall temperature [25]. Fig. 11 shows the mean
 402 standard deviation of all the measured wall temperatures as a function of the
 403 Reynolds number. For low Reynolds numbers the standard deviation is low
 404 and corresponds to the measurement noise. A significant increase for $Re >$
 405 160 indicates the onset of the transitional regime, when the flow pulsation
 406 allows the colder central stream to contact the wall regions, increasing the
 407 wall temperature fluctuations. Above $Re = 300$, the value is higher than
 408 in the laminar region but stable again, pointing the onset of the turbulent
 409 regime.

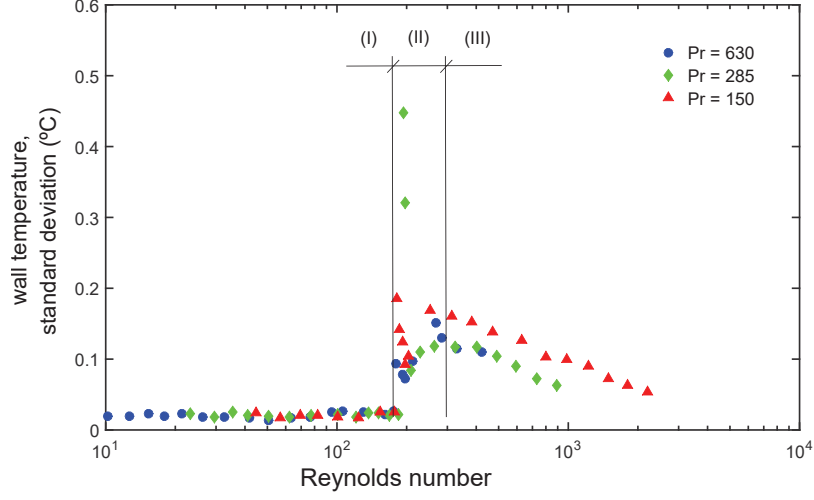


Figure 11: Standard deviation of the wall temperature vs Reynolds number.

410 *Performance evaluation.*

411 In order to evaluate the thermal enhancement of the geometry tested, the
 412 R3 criterion is used [26]. This parameter measures the heat transfer ratio
 413 between the tested geometry and an equivalent smooth tube for the same
 414 power consumption and basic geometry (number of tubes and tube diameter
 415 and length) (Eq. 9).

$$R3 = \frac{Nu}{Nu_s} \Bigg|_{\dot{W}=\dot{W}_s, N=N_s, D=D_s, l=l_s} \quad (9)$$

416 For the same power consumption, well-known correlations of Nusselt number
 417 for the laminar [27] and turbulent [28] regions are used for calculating the
 418 term Nu_s . The results for $Pr = 150$ are represented in Fig. 12.

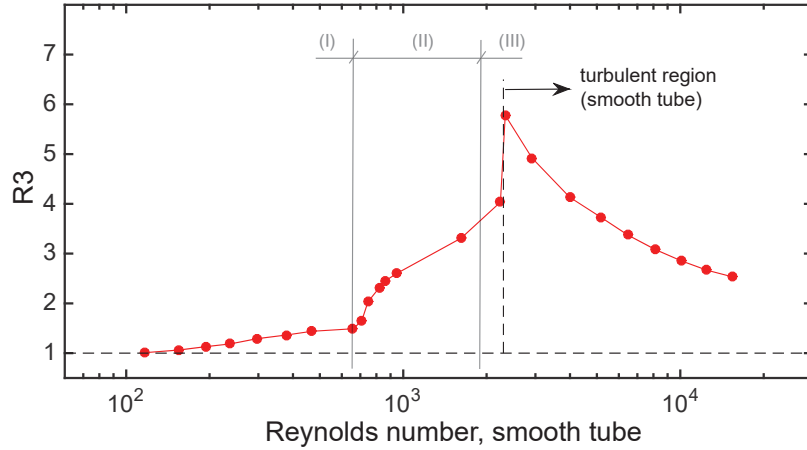


Figure 12: Performance evaluation criteria R3 vs smooth tube Reynolds number, $Pr = 150$.

419 As can be observed, the circular-orifice baffles show a poor performance
 420 for $Re_s < 700$, and a slight increase in the thermal performance with the
 421 Reynolds number. This is due to the increase in the Nusselt number in the
 422 laminar region when the Re is increased. Above $Re_s = 800$ there is a sharp
 423 rise in the thermal performance due to the onset of the transitional regime
 424 in the baffled tube. So, the range $800 < Re_s < 2300$ is where the highest
 425 performance can be expected. This trend is cut by the onset of the tran-
 426 sitional regime in the smooth tube at $Re_s = 2300$, generating a descending
 427 trend in the performance. However, there is enhancement for all the range
 428 tested, with the lowest performance, R3 2.5, at $Re_s \approx 2 \times 10^4$.

429 7. Conclusions

- 430 1. An extensive study has been done in order to quantify the thermo-
 431 hydraulic performance of tubes with periodically-spaced circular-orifice

- 432 baffles. A wide range of dimensionless numbers has been studied ($Pr =$
433 $150 - 630$, $Re_n = 10 - 2200$).
- 434 2. Qualitative flow visualization tests show the flow patterns in the baffled
435 tube in the three different flow regimes. In the laminar region, the
436 size of the recirculation zones under the baffles characterizes the flow.
437 Instability can be observed for $Re > 160$, this instability of the flow is
438 related to the pulsation of the core stream. For a $Re > 300$ the flow
439 can be described as chaotic.
- 440 3. Pressure drop and heat transfer measurements demonstrate the exis-
441 tence of three flow regions with distinguishable characteristics: a lam-
442 inar region ($Re < 160$), a transitional region ($160 < Re < 300$) and a
443 turbulent region ($Re > 300$).
- 444 4. The $R3$ performance criteria shows that the tested geometry can be
445 advantageous, for $Pr = 150$, in comparison to smooth tubes working
446 at a Reynolds number between 100 and $2 \cdot 10^4$.

447 **Acknowledgements**

448 The authors gratefully acknowledge the financial support of the project DPI2015-
449 661943-P by Ministerio de Economía y Competitividad (MINECO, Spain)
450 and the Fondo Europeo de Desarrollo Regional (FEDER). The authors are
451 grateful to SEDIC-SAIT (UPCT) for providing the technical resources for
452 CFD computations.

453 **8. References**

- 454 [1] R. Manglik, A. Bergles, Heat transfer and pressure drop correlations for
455 twisted tape inserts in isothermal tubes: Part I Laminar flows, *Journal*
456 *of Heat Transfer* 115 (4) (1993) 881–889.
- 457 [2] R. Manglik, A. Bergles, Heat Transfer and Pressure Drop Correlations
458 for Twisted-Tape Inserts in Isothermal Tubes: Part II Transition and
459 Turbulent Flows, *Journal of Heat Transfer* 115 (4) (1993) 890–896.
- 460 [3] S. M. Abolarin, M. Everts, J. P. Meyer, Heat transfer and pressure drop
461 characteristics of alternating clockwise and counter clockwise twisted
462 tape inserts in the transitional flow regime, *International Journal of*
463 *Heat and Mass Transfer* 133 (2019) 203–217.
- 464 [4] T. Ravigururajan, A. Bergles, Development and verification of general
465 correlations for pressure drop and heat transfer in single-phase turbulent
466 flow in enhanced tubes, *Experimental Thermal and Fluid Science* 13 (1)
467 (1996) 55–70.
- 468 [5] A. Garcia, P. G. Vicente, A. Viedma, Experimental study of heat trans-
469 fer enhancement with wire coil inserts in laminar-transition-turbulent
470 regimes at different Prandtl numbers, *International Journal of Heat and*
471 *Mass Transfer* 48 (21-22) (2005) 4640–4651.
- 472 [6] P. Drögemüller, The Use of hiTRAN Wire Matrix Elements to Im-
473 prove the Thermal Efficiency of Tubular Heat Exchangers in Single and
474 TwoPhase Flow, *Chemie Ingenieur Technik* 87 (3) (2015) 188–202.

- 475 [7] V. Kongkaitpaiboon, K. Nanan, S. Eiamsa-ard, Experimental investiga-
476 tion of convective heat transfer and pressure loss in a round tube fitted
477 with circular-ring turbulators, *International Communications in Heat
478 and Mass Transfer* 37 (5) (2010) 568–574.
- 479 [8] P. Promvonge, N. Koolnapadol, M. Pimsarn, C. Thianpong, Thermal
480 performance enhancement in a heat exchanger tube fitted with inclined
481 vortex rings, *Applied Thermal Engineering* 62 (1) (2014) 285–292.
- 482 [9] A. Acir, I. Ata, M. E. Canli, Investigation of effect of the circular ring
483 turbulators on heat transfer augmentation and fluid flow characteristic
484 of solar air heater, *Experimental Thermal and Fluid Science* 77 (2016)
485 45–54.
- 486 [10] K. Ruengpayungsak, K. Wongcharee, C. Thianpong, M. Pimsarn,
487 V. Chuwattanakul, S. Eiamsa-ard, Heat transfer evaluation of turbu-
488 lent flows through gear-ring elements, *Applied Thermal Engineering* 123
489 (2017) 991–1005.
- 490 [11] S. Eiamsa-Ard, V. Kongkaitpaiboon, K. Nanan, Thermohydraulics of
491 turbulent flow through heat exchanger tubes fitted with circular-rings
492 and twisted tapes, *Chinese Journal of Chemical Engineering* 21 (6)
493 (2013) 585–593.
- 494 [12] S. M. Abolarin, M. Everts, J. P. Meyer, The influence of peripheral u-
495 cut twisted tapes and ring inserts on the heat transfer and pressure drop
496 characteristics in the transitional flow regime, *International Journal of
497 Heat and Mass Transfer* 132 (2019) 970–984.

- 498 [13] X. Ni, M. Mackley, A. Harvey, P. Stonestreet, M. Baird, N. Rama Rao,
499 Mixing Through Oscillations and Pulsations A Guide to Achieving Pro-
500 cess Enhancements in the Chemical and Process Industries, Chemical
501 Engineering Research and Design 81 (3) (2003) 373–383.
- 502 [14] M. R. Mackley, P. Stonestreet, Heat Transfer and Associated Energy
503 Dissipation for Oscillatory Flow in Baffled Tubes, Chemical Engineering
504 50 (14) (1995) 2211–2224.
- 505 [15] Paste Particle and Polymer Processing group (P4G), Oscillatory Fluid
506 Mixing. OFM: Enhancement of heat transfer rates.
- 507 [16] R. Law, S. Ahmed, N. Tang, A. Phan, A. Harvey, Development of a
508 more robust correlation for predicting heat transfer performance in os-
509 cillatory baffled reactors, Chemical Engineering and Processing - Process
510 Intensification 125 (December 2017) (2018) 133–138.
- 511 [17] D. González-Juárez, R. Herrero-Martín, J. P. Solano, Enhanced heat
512 transfer and power dissipation in oscillatory-flow tubes with circular-
513 orifice baffles: a numerical study, Applied Thermal Engineering
514 141 (January) (2018) 494–502.
- 515 [18] R. Kiml, A. Magda, S. Mochizuki, A. Murata, Rib-induced secondary
516 flow effects on local circumferential heat transfer distribution inside a
517 circular rib-roughened tube, International Journal of Heat and Mass
518 Transfer 47 (6-7) (2004) 1403–1412.
- 519 [19] J. Muñoz, D. Crespi, J. P. Solano, P. G. Vicente, On the early onset of
520 transition in circular-orifice baffled tubes : an experimental study, in:

- 521 Proceedings of the Ninth International Symposium on Turbulence, Heat
522 and Mass Transfer, 2018, pp. 561–564.
- 523 [20] A. C. Jealous, H. F. Johnson, Power Requirements for Pulse Generation
524 in Pulse Columns, *Industrial & Engineering Chemistry* 47 (6) (2005)
525 1159–1166.
- 526 [21] F. Johansen, Flow through Pipe Orifices at Low Reynolds Numbers,
527 *Proceedings of the Royal Society of London* 126 (801) (1930) 231–245.
- 528 [22] X. Ni, G. Brogan, A. Struthers, D. C. Bennett, S. F. Wilson, A sys-
529 tematic study of the effect of geometrical parameters on mixing time in
530 oscillatory baffled columns, *Chemical Engineering Research and Design*
531 76 (A5) (1998) 635–642.
- 532 [23] E. N. Sieder, G. E. Tate, Heat transfer and pressure drop of liquids in
533 tubes, *Industrial & Engineering Chemistry* 28 (12) (1936) 1429–1435.
- 534 [24] ISO, Guide to the Expression of Uncertainty in Measurement, 1st Edi-
535 tion, International Organization for Standardization, Switzerland, 1995.
- 536 [25] J. P. Meyer, S. M. Abolarin, Heat transfer and pressure drop in the
537 transitional flow regime for a smooth circular tube with twisted tape
538 inserts and a square-edged inlet, *International Journal of Heat and Mass*
539 *Transfer* 117 (2018) 11–29.
- 540 [26] A. Bergles, A. Blumenkrantz, J. Taborek, Performance evaluation cri-
541 teria for enhanced heat transfer surfaces, in: *Proceedings of the 5th*
542 *International Heat Transfer Conference, Vol. 2, Tokyo, Japan, 1974*, pp.
543 239–243.

- 544 [27] B.S. Petukhov; A. F. Polyakov, Heat Transfer in Laminar Mixed Con-
545 vection, 1st Edition, Hemisphere, New York, 1988, Ch. 3, pp. 57–89.
- 546 [28] V. Gnielinski, New Equations for Heat and Mass Transfer in Turbu-
547 lent Pipe and Channel Flow, International Chemical Engineering 16 (2)
548 (1976) 359–368.